

Investigations of Heme Protein Absorption Line Shapes, Vibrational Relaxation, and Resonance Raman Scattering on Ultrafast Time Scales[†]

Xiong Ye, Andrey Demidov, Florin Rosca, Wei Wang, Anand Kumar, Dan Ionascu, Leyun Zhu, Doug Barrick,[‡] David Wharton, and Paul M. Champion*

Physics Department and Center for Interdisciplinary Research on Complex Systems, Northeastern University, Boston, Massachusetts 02115

Received: December 10, 2002

The spectral dynamics of photoexcited myoglobin (Mb) and its ligated species have been measured using both single wavelength and broadband continuum probes. Ultrafast spectral relaxation of the deoxy photoproduct involves an initially broadened and red-shifted absorption band, which is observed for all samples studied (deoxyMb, metMb, MbNO, MbCO). These results are consistent with an immediate (sub 100 fs) relaxation to the electronic ground state followed by vibrational equilibration. Relaxation of the “hot” photoproduct spectrum is well described using independent time scales for narrowing (400 fs) and blue shifting (0.4–4 ps) as the system returns to equilibrium. A previous multiple electronic intermediate state model, which is based on single wavelength measurements (Petrich, J. W.; Poyart, C.; Martin, J. L. *Biochemistry* **1988**, *27*, 4049), does not adequately explain the observed broadband spectral dynamics, particularly on the blue side of the Soret band (unless still more electronic states are postulated). The vibrational relaxation pathway in Mb is explored by using samples with a modified local heme environment (e.g., His93 → Gly mutation and protoporphyrin IX → porphine substitution). The His93 → Gly mutation experiment demonstrates that the covalent bond between the iron and the proximal histidine has little effect on the overall vibrational relaxation of the “hot” heme. In contrast, the protoporphyrin IX → porphine substitution experiment demonstrates the importance of the van der Waals contacts between the heme and the protein/solvent matrix in cooling the locally hot heme. Finally, we discuss the effects of the observed broadband spectral dynamics on time-resolved resonance Raman intensities and show how the time dependent line shape function plays an important role in the extraction of mode specific vibrational temperatures from the resonance Raman data.

I. Introduction

Myoglobin (Mb) is a prototypical heme protein that can reversibly bind small ligands such as O₂, CO, and NO.¹ Its role as the oxygen storage protein in muscle cells is well established and it has recently been proposed to be involved in controlling NO concentrations in heart and skeletal muscle cells.^{2–4} Myoglobin has been shown to dissociate its diatomic ligand nearly instantaneously upon photoexcitation^{5–9} and this has made the Mb system the focus of a variety of kinetic studies.^{10–17} Photolysis using ps or fs laser pulses rapidly prepares an initial nonequilibrium heme/protein state and a separated heme–ligand pair, which allows the ensuing fast ligand rebinding and heme/protein conformational relaxation processes to be studied with suitably delayed laser probe pulses.^{9,12,15,18,19} Since the photon energy is initially localized on the heme and the dissociated ligand, an account of the energy flow not only helps decouple the various processes, but also serves as a model system for studying the energy relaxation path in complex molecules.^{20–24} For example, time-resolved Raman spectroscopy has been used to study vibrational mode-specific relaxation processes after photoexcitation.^{22,25–27} Time-resolved Raman spectroscopy has the advantage of studying individual vibrational modes, but the time resolution is limited

to picosecond and longer time scales due to the need for a relatively narrow frequency distribution ($<10\text{--}20\text{ cm}^{-1}$) in the probe laser pulse.

On the other hand, subpicosecond transient absorption studies of myoglobin in the Soret band,^{9,19,28,29} Q-band,³⁰ and band III³¹ regions have also been reported. These studies revealed complex ultrafast relaxation dynamics. The interpretation of the measurements has been based upon two distinct models: (1) the *vibrationally* excited (“hot”) electronic ground-state model^{19,30} or (2) the multiple *electronic* intermediate excited-state model.^{9,29,31,32} The present work offers strong evidence in favor of model 1, the vibrationally hot electronic ground-state model. In support of this assertion, we present a detailed analysis of the time evolution of the absorption line shape in the Soret band region of Mb following optical excitation. This analysis helps to delineate the relationship between the dynamic line shape and the transient response measured at fixed wavelengths.⁹ We find that the optical transients are characteristic of an initially broad and red-shifted “hot” electronic ground-state photoproduct spectrum, which narrows and blue-shifts as it relaxes to equilibrium.

Similar red-shifted absorption spectra have been observed for other molecular systems upon photoexcitation^{33,34} and assigned to vibrationally hot species. The most extensive and relevant work is that of Holton et al. on various metal porphyrin molecules such as nickel tetraphenylporphyrin (NiTPP), magnesium octaethylporphyrin (MgOEP), zinc porphyrin with

[†] Part of the special issue “A. C. Albrecht Memorial Issue”.

* Corresponding author. E-mail: champ@neu.edu.

[‡] Department of Biophysics, Johns Hopkins University, Baltimore, MD 21218.

quinone (ZnP-Q), and free base tetraphenylporphyrin (H₂TPP), among others.^{35–38} In these “model” systems, the initial photo-product spectra were observed to be red-shifted and broadened, followed by subpicosecond and picosecond processes that narrow and shift the line shape back to the initial equilibrium spectra. These observations were explained on the basis of the rapid creation of a vibrationally “hot” photoproduct state, arising from the photon excitation energy. Vibrational excitation of the ground electronic state of the heme is taken as the cause of the broadening and red shift of the transient absorption spectrum. Subsequent vibrational relaxation and cooling allows the “hot” absorption spectrum to evolve toward equilibrium.

To explore the pathway of vibrational energy relaxation, we also study the spectral dynamics as the heme structure and local environment are altered. Consistent with recent molecular dynamics simulations,²⁴ the experimental results suggest that the van der Waals interactions between the heme and the protein matrix provide the main relaxation pathway for dissipation of the excess vibrational energy.

II. Experimental Methods and Materials

Sample Preparation. Horse heart myoglobin was obtained from Sigma Inc. The His93 → Gly (H93G) myoglobin mutant was expressed in *Escherichia coli* and purified as described in detail elsewhere.³⁹ The H93G mutant with an exogenous proximal imidazole ligand was prepared using standard procedures.⁴⁰ Porphine was purchased from Porphyrin Products Inc. Iron–porphine and its reconstitution with apomyoglobin was carried out as previously described.⁴¹ MetMb solutions were prepared using 100 mM potassium phosphate buffer (pH 7.0) at room temperature. Typically, a metMb solution was degassed with argon for 1 h and an equimolar quantity of 1 M sodium dithionite was added to obtain deoxyMb. MbNO was prepared by further addition of an equimolar quantity of 1 M degassed sodium nitrite solution to the deoxyMb sample with excess sodium dithionite. MbCO was prepared by flushing CO gas over the surface of the deoxyMb sample for 1 h. In all cases, the sample concentration was adjusted to have a Soret peak absorption of ca. 1 OD in a 1 mm path length cell. The absorption spectra were measured before and after each experiment with a spectrophotometer (Hitachi U-3410) to check sample quality and stability. All samples were placed in an anaerobic spinning cell having a 2-in. diameter and a 1 mm path length. The cell was rotated at about 7000 rpm using a brushless high tolerance motor (Maxon Precision Motors, Inc.).

Single Wavelength Optical Transient Measurements. “Single” wavelength optical transient measurements were performed with a Ti:sapphire laser, MIRA 900 (Coherent Inc.), which generated 45–80 fs laser pulses in the wavelength range 760–960 nm. The pulses came with a repetition rate of 76 MHz and were focused into a 0.2 mm thick BBO crystal to generate second harmonic pulses in the 380–480 nm range. The laser beam was directed to a double pass prism pair for chirp compensation to obtain near transform limited laser pulses at the sample. (Since the pulses were transform limited, the “wavelength” corresponds to the optical carrier frequency, and typical pulses were 7–8 nm in width, much smaller than the absorption bands under study). Finally, the pulse train is split in two parts in a 3/2 ratio to be used as the pump and probe beams.

The polarization of the pump beam is rotated by 90° using a half-wave plate. The polarization rotation was used to better suppress the pump beam “leakage” in the detection step (see below). The pump beam passed through an acousto-optic

modulator (NEOS, Inc.) that modulated (or “chopped”) the beam at 1.5 MHz. The chopping frequency was controlled by a lock-in amplifier (SRS 844, Stanford Research, Inc.). The probe beam traveled an optical path comparable with the path of the pump beam. The exact delay between the pump and probe pulse pairs was controlled by a motorized translation stage (Klinger, Inc.). Both pump and probe beams were combined in the sample using a lens with 2 in. focal length. Measurements showed that the beams were focused to a diameter of approximately 20–30 μm. The average power of the pump beam at the sample was about 30 mW, whereas for the probe beam it was about 20 mW. The excitation pulse energy was sufficiently low that only ca. 1–2% of the sample was photolyzed by each pulse.

After the sample, the pump beam was extinguished using a spatial filter and a crossed polarizer. The pump beam must be suppressed because the pump-induced change in the transmission intensity of the probe beam was about 10⁻⁴–10⁻⁵ and leakage of the pump pulses into the detection channel gives a significant increase in the background offset of the detected signal. The probe beam was directed to a photodiode connected to the lock-in-amplifier. The lock-in-amplifier and the controller of the motorized translation stage were connected to a computer via a GPIB interface. Data acquisition is performed with self-developed software based on the Labview language (National Instruments, Inc.).

Continuum Spectral Measurements. Although the single wavelength measurements provide the optimum signal-to-noise in the time domain, it is also important to record the spectrum of the full absorption band in the frequency domain using continuum pulses. To measure transient spectra over a wide wavelength range, we used another laser system based on an amplified Ti:sapphire laser (REGA 9050, Coherent, Inc.) with white light continuum generation. Details and schematics of this system can be found elsewhere.^{19,42} The amplified laser system generated ~50 fs laser pulses at ~800 nm with a repetition rate of 250 kHz and an average power of ~1 W. It then passed through a beam splitter and one beam feeds an optical parametric amplifier (OPA 9400, Coherent, Inc.) to get pulses at 580 nm used for pumping the sample. The other beam generated the white light probe pulse continuum in a spinning fused silica disk. The continuum spectrum covers a range from 390 to over 800 nm and the blue part (<500 nm) was selected by a cutoff filter. Another blue glass filter was applied to flatten the probe spectrum so that the dynamic range of the continuum does not exceed the detection limits. The OPA pulses were compressed by a prism pair to about 50 fs. As with the single wavelength measurements, the time delay between the pump and probe pulses was controlled by a motorized translation stage (Melles Griot, Inc.). The pump and probe beams were focused into the spinning sample cell using an achromatic lens with a 2-in. focal length. At the sample, the average powers were ~10 mW for the OPA pump beam and ~10 μW for the white light continuum probe beam (integrated over the bandwidth 400–500 nm). The detection was based on a lock-in amplifier technique where the pump beam was chopped by a mechanical chopper (3 kHz) and a photomultiplier tube (PMT) was used to detect the probe light as the wavelength is scanned by the monochromator. The detected signal was proportional to both the pump-induced absorption change and the probe light intensity. Thus, we used a light stabilizer (Cambridge Research & Instrumentation) that adjusted the probe light power to keep a constant average photocurrent as the monochromator was scanned across the detection wavelengths. This works by using the DC part of the PMT output as the feedback control to the light stabilizer.

Because of the well-known effect of “chirp”, different colors of the white light continuum arrived at the sample at different time delays. Unfortunately, the breadth of the spectral range ($\sim 100\text{--}150\text{ nm}$) made it very difficult to compensate the chirp using prisms or gratings. However, we measured the chirp profile separately and then compensated for the wavelength dependent time zero point by using software to simultaneously control the translation stage time delay and the monochromator grating position. The chirp profile was found by measuring the coherence coupling response as a function of wavelength using pure water placed in the sample cell. The coordinates $[\lambda, t_0]$ that define the maxima of the water coherence coupling peak were fit by a polynomial to obtain the chirp profile that sets time zero for each wavelength.

Maximum Entropy Method. The majority of the single wavelength optical transient data reported here were analyzed using the maximum entropy method (MEM). In contrast to standard nonlinear least squares, which fit the data to a set (n) of discrete exponentials,

$$I(t) = \sum_{i=0}^n c_i \exp(-t/\tau_i) \quad (1)$$

MEM recovers a distribution of amplitudes in rate space, essentially performing a numerical inverse Laplace transform on the experimental data

$$I(t) = \int_0^\infty g(\lambda) e^{-\lambda t} d\lambda \quad (2)$$

For details, we refer the reader to the literature related to the MEM method.^{43–46} The big advantage of the MEM analysis is that the addition of the entropy function helps to extract a *unique* solution for the rate distribution that is free of unwanted correlations. Since MEM does not require any preassumption of the expected rate distribution, it is said to be maximally noncommittal with respect to unavailable information.

III. Results and Analysis

Single Wavelength Measurements of Photoexcited MbNO and deoxyMb. In Figure 1 we show “single” wavelength optical transients of MbNO using the unamplified laser setup. The optical transients were measured using optical carrier frequencies between 385 and 470 nm. The right panels display the MEM analysis of the data, where we note that the decay of bleaching and the rise of antibleaching signals (transmission decrease with time) are represented by positive amplitudes and the decay of antibleaching and the rise of bleaching signals (transmission increase with time) are represented by negative amplitudes. Note that at 385 nm, the signal clearly shows the decay of an antibleach. Optical transients in the 400–425 nm region show a bleaching signal (transmission change is shown). At around 430 nm we observe a transition of the signal from the bleaching back to the antibleaching region, where it remains during the recovery phase. Between 435 and 454 nm only antibleaching signals are recorded, while the optical transients measured at 460 and 470 nm show an antibleach that evolves into a bleaching signal on longer ($> 10\text{ ps}$) time scales. We note that the equilibrium difference spectrum (Mb – MbNO) has three isosbestic points near 398, 427, and 455 nm, which explains the evolution to a bleaching signal at 460 nm and 470 nm (cf. Figure 9).

Practically all of the optical transients are characterized by both fast and slow time components. The MEM analysis reveals that they can be clustered into four major groups: $< 0.1, 0.3\text{--}$

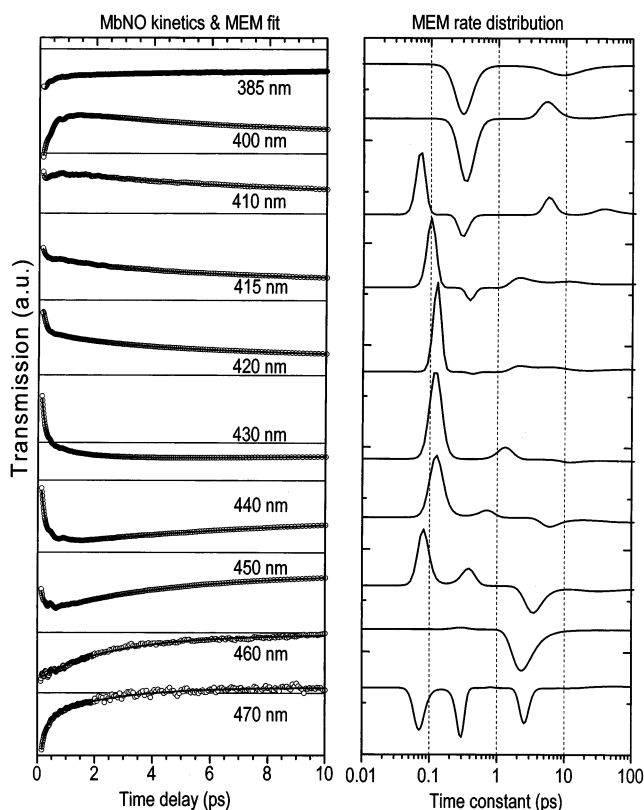


Figure 1. MbNO optical transients measured with the single wavelength technique. The right panel shows the corresponding rate distribution calculated using the maximum entropy method (MEM). In both Figures 1 and 2, the ordinate represents transmittance and is given in arbitrary units. For the rate distribution, the decay of bleaching and the rise of antibleaching signals (transmission decrease with time) are represented by positive amplitudes and the decay of antibleaching and the rise of bleaching signals (transmission increase with time) are represented by negative amplitudes.

1, 2–4, and $> 10\text{ ps}$ clusters. On the longer time scale ($> 10\text{ ps}$, data not shown), the rate distribution is independent of probe wavelength and can thus be attributed to rebinding kinetics rather than spectral dynamics.¹⁹ On shorter time scales, the ultrafast optical transients of MbNO show similar behavior as with other ligated samples of myoglobin and model compounds, i.e., the relaxation strongly depends on the probe wavelength. As we discuss below, the wavelength dependent short time behavior is difficult to explain using the multiple electronic state model (model 2), but relatively easy to explain using the vibrationally hot electronic ground-state model (model 1).

In Figure 2 we present the single wavelength optical transients and MEM analysis of deoxy Mb. Note that these data have features similar to the MbNO sample, despite the absence of photolysis in deoxyMb (a five coordinate species). In the case of deoxyMb, we group the time constants into two major clusters: 0.1–0.5 and 2–6 ps. All the optical transients in Figures 1 and 2 are presented in arbitrary units of transmission change (ΔT).

Continuum Transient Spectra of Photoexcited DeoxyMb, MetMb, MbCO. DeoxyMb contains a pentacoordinate ferrous heme, and metMb has a hexa-coordinate ferric heme, with a water molecule weakly bound as the sixth ligand. The corresponding Soret peaks for deoxyMb and metMb are 434 and 409 nm, respectively. For a pentacoordinate ferric heme (without the water molecule) the Soret peak shifts from 409 to 394 nm.⁴⁷ The continuum absorption measurement of metMb does not detect an antibleach band increase in ΔA near 394 nm upon

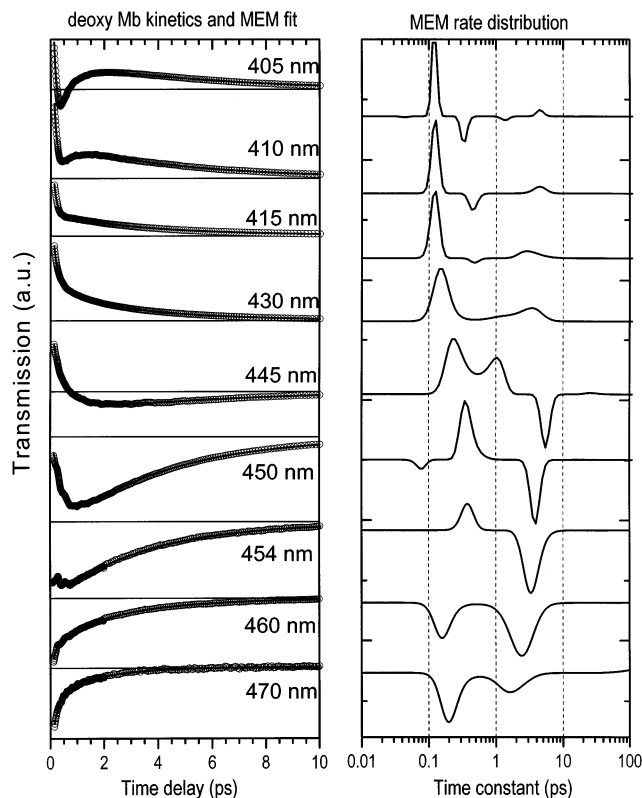


Figure 2. DeoxyMb optical transients measured with the single wavelength technique. The right panel shows the corresponding rate distribution calculated with the maximum entropy method (MEM).

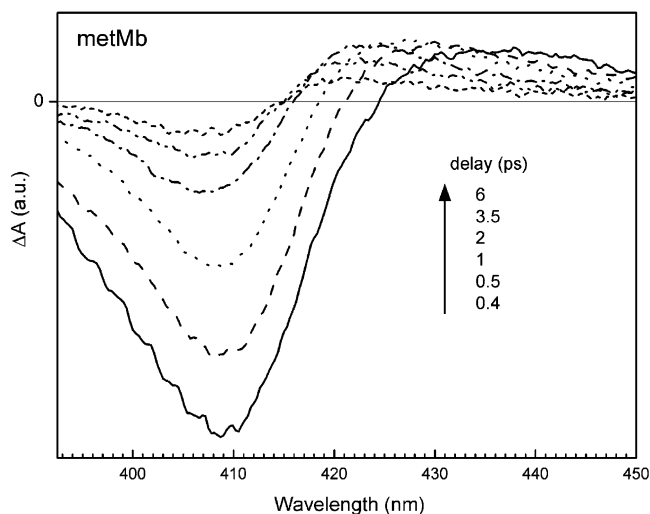


Figure 3. Transient absorption spectra of metMb pumped at 580 nm and probed with the continuum.

photoexcitation (Figure 3). This implies that dissociation of the water molecule does not take place after photoexcitation. Thus, in both deoxy and met myoglobin, photon energy is converted to heme vibrational energy. This results in an extremely hot heme. For example, it was estimated that for 530-nm excitation of heme proteins at room temperature, the local heme temperature is raised by 500–700 K.⁴⁸

The broadband continuum probe yields very similar ultrafast spectral dynamics for both metMb (Figure 3) and deoxyMb (Figure 4). Both show an almost instantaneous appearance of a broad antibleach (absorption) to the red of the equilibrium Soret band. The peak and isosbestic point (zero crossing of ΔA) shift to the blue as time proceeds. Since the transient spectrum measures the difference between the photoproduct and

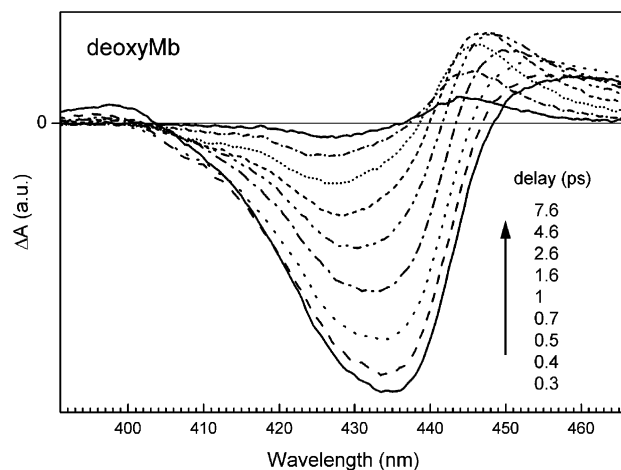


Figure 4. Transient absorption spectra of deoxyMb pumped at 580 nm and probed with the continuum.

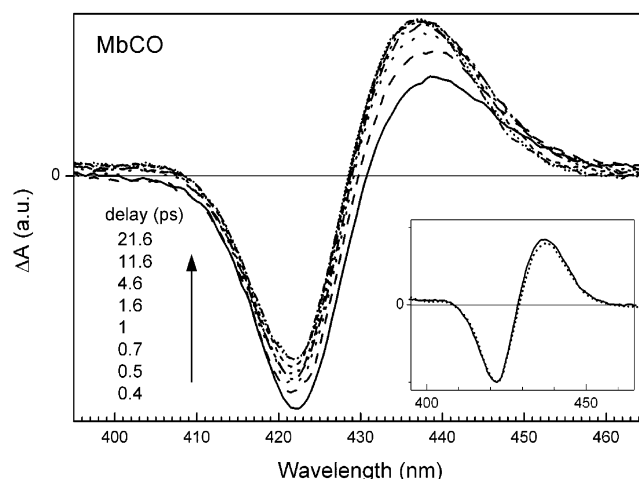


Figure 5. Transient absorption spectra of MbCO pumped at 580 nm and probed with the continuum. The inset compares the line shape at 21.6 ps (solid line) with the equilibrium difference spectrum of deoxyMb and MbCO (dotted line).

the initial equilibrium spectra, and there is no photolysis for these samples, the dynamics of the transient spectrum effectively arises from the spectral evolution of the photoexcited system. For a simple two-state photolysis reaction with no spectral evolution, the transient absorption line shape is simply composed of an amplitude decay with a fixed isosbestic point and a line shape profile composed of the equilibrium (static) product and reactant difference spectra. In addition to the simple two-state ligand rebinding process, a hot photoproduct spectrum can show dynamic evolution as seen in Figures 3 and 4 (where no photolysis has taken place). The classic signature of thermal relaxation involves a broadened and red-shifted absorption band that undergoes spectral narrowing and blue shifting. This manifests itself as a time-dependent blue shift of the “isosbestic” point (i.e., the zero crossing of ΔA) in the transient difference spectrum as seen in Figures 3 and 4.

Figure 5 shows transient spectra of MbCO using 580-nm excitation, which induces dissociation of the CO ligand. The photodissociation yield of CO has been measured to be unity,⁴⁹ resulting in only one type of photoproduct species, the dissociated pentacoordinate heme. However, since photon energy in excess of the dissociation energy is deposited in the heme–ligand pair, the photolysis process also generates a hot deoxy heme species. This species undergoes vibrational relaxation that is detectable because CO geminate recombination to the iron

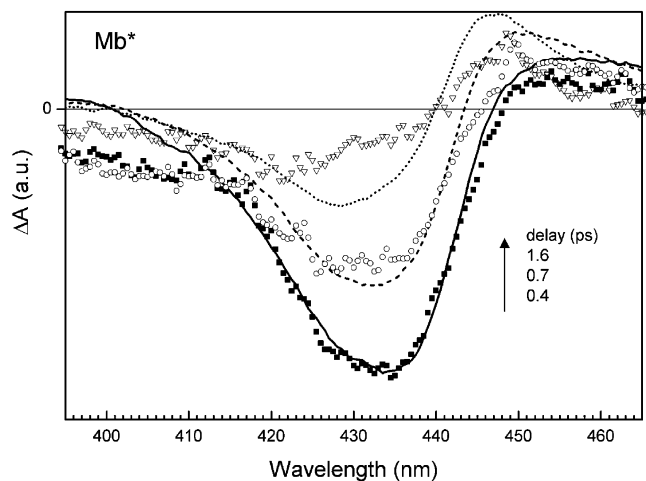


Figure 6. The dynamic part of the MbCO transient spectrum (open symbols) calculated by subtracting the transient spectrum measured at 21.6 ps from the transient spectra measured at 0.4, 0.7, and 1.6 ps. It is assumed that, at the 21.6 ps delay, all cooling and vibrational relaxation processes are complete and the observed transient spectrum contains only the static equilibrium difference (CO does not rebind on this time scale). The solid and dashed lines represent the transient spectra of deoxyMb measured at the same time delays. Excitation is at 580 nm.

atom takes place on a relatively slow (10–100 ns) time scale¹⁴ and does not interfere with signals arising from the spectral dynamics of heme cooling.

We observe that the transient spectrum measured at 20-ps delay is almost identical to the difference spectra of equilibrium deoxyMb and MbCO (see inset of Figure 5). This means that the ultrafast dynamics of the photoproduct spectra due to localized heme relaxation processes are completed by 20 ps. Thus, by subtracting the “static” difference spectrum measured at 20 ps from the earlier transient difference spectra, we obtain the transient spectral dynamics of the deoxy photoproduct without the “static” background (see Figure 6). Comparing the result with the transient spectra measured for deoxyMb (solid lines and data points in Figure 6), it can be seen that there is a reasonable match between the MbCO photoproduct and the deoxyMb transient spectra. This observation supports the view that the MbCO photoproduct, Mb*, involves a vibrationally hot heme, which is analogous to the photoexcited deoxy Mb. The subsequent relaxation of Mb* provides the major source of dynamics in the transient spectra of MbCO (e.g., the small short time dynamics in Figure 5 observed near 423 nm in the region of the MbCO bleach is due to relaxation of the blue side of the Mb* Soret band, not to CO rebinding).

We can also reconstruct the absolute MbCO photoproduct spectrum representing Mb*. This is again facilitated by the long recombination time of photodissociated CO, so that complications due to CO recombination are absent. The reconstruction was made by summing the transient difference spectrum with a scaled equilibrium spectrum of MbCO. The scaling factor is obtained by fitting the equilibrium difference spectrum of deoxyMb and MbCO with the transient spectrum measured at 20 ps delay. The transient spectra of Mb* reveal that the photoproduct spectrum is broadened and red-shifted at the earliest times, followed by evolution toward the equilibrium spectrum of deoxyMb (Figure 7). This type of behavior after nearly instantaneous photolysis is characteristic of a vibrationally “hot” deoxyMb in the ground electronic state. The “temperature” associated with this vibrational excitation is local and can be relatively high. The reconstructed spectra reveal cooling of Mb*,

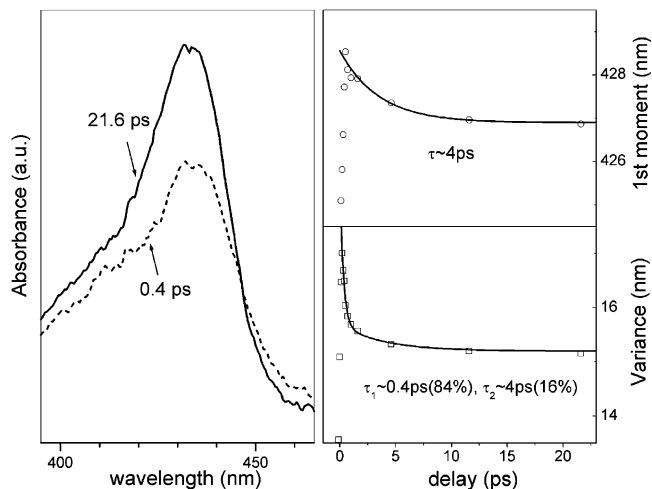


Figure 7. Reconstructed spectra of the photoproduct of MbCO excited at 580 nm. The right panel shows the relaxation of the first moment and variance.

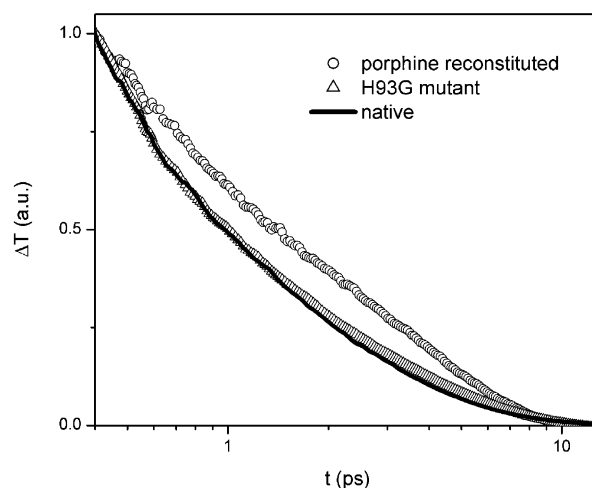


Figure 8. Optical transients of native myoglobin, porphine-reconstituted myoglobin, and H93G mutant myoglobin (note log scale). The samples are in the deoxy form and are probed at their respective Soret peaks.

as manifested by the narrowing of the absorption spectrum. After calculating the time dependence of the first moment and variance of the spectra, we can adequately fit their relaxation with exponential decays. We find that the time constant for spectral narrowing has a fast phase of 400 fs with 84% amplitude and a 4 ps phase with 16% amplitude, while the first moment evolves with a single 4 ps time constant (Figure 7). The 400 fs to 4 ps components of the spectral evolution potentially involve both intramolecular, non-Boltzmann, vibrational redistribution processes and “cooling” of a hot, Boltzmann equilibrated heme via vibrational energy transfer between the heme and the protein/solvent heat bath.²¹

Optical Transients of Mutant Mb (H93G) and Porphine Reconstituted Mb. We next consider the effect of different heme-localized perturbations on the vibrational relaxation pathway of deoxy heme. The probe-wavelength dependence of the optical transients potentially complicates such comparisons, so in Figure 8 we compare the transient response probed at the Soret peak of each compound (deoxyMb, deoxyMbH93G bound with imidazole (Im), and porphine-substituted Mb). MbH93G has the proximal histidine (H93) replaced with a glycine residue. This effectively disconnects the only covalent bond between the heme and the protein matrix. In MbH93G+Im, an exogenous

imidazole ligand is added and bound to the iron at the proximal side to stabilize the deoxy sample.^{39,40} The porphine-substituted Mb contains a heme where all the protoporphyrin IX side chains are replaced by protons.

The transient relaxations of all three compounds are completed within 10 ps (Figure 8), where it can be seen that the optical transient of H93G is quite similar to that of native deoxyMb. On the other hand, the optical transient of the porphine-reconstituted myoglobin has slower relaxation than that of native deoxyMb. This rules out the possibility that covalent bonding to the protein matrix, through the Fe–His bond, offers a significantly more efficient vibrational relaxation pathway for the hot heme than the noncovalent interactions between the heme and its protein surroundings.

When studying vibrational relaxation, we usually consider the heme to be a separate thermal bath separated from that of the protein matrix. Although the iron is covalently linked to the proximal histidine, the Fe–N_{His} bond is orthogonal to the heme plane and probably decoupled from many of the in-plane heme normal modes that are coupled to the optical excitation and initial nonradiative decay. This may help to explain why the covalent axial ligand connection between the heme iron and the protein is not a dominant vibrational relaxation pathway for the hot heme, as demonstrated by H93G kinetics data. In contrast, prior studies of Fe–His coherence⁵⁰ indicate that energy is dissipated from the Fe–His mode into the heme heat bath with a periodicity (800 fs) that is coincident with the 40 cm⁻¹ mode associated with heme doming. Evidently, this energy flow is essentially a “one-way” process, with entropic considerations preventing the reverse process of energy flow from the heme back through the single Fe–His bond and into the protein.

On the other hand, the protein backbone of Mb folds and forms a hydrophobic pocket that helps to hold the heme in place. This allows the heme to couple to the protein through van der Waals contacts. These interactions, and those between the propionates and solvent water, apparently provide the main relaxation pathway for the hot heme.²⁴ The side chain structure of the heme should affect the strength of such contacts. In porphine-reconstituted myoglobin, we expect the contacts to become weaker, since all of the side chains are replaced by protons. This suggests that the vibrational relaxation will be slower, as is confirmed by the experimental data in Figure 8. It has also been suggested²⁴ that the strong electrostatic interaction between propionate side chain and solvating water is the most important “doorway” for dissipation of excess heme kinetic energy. Although precise verification of the side chain specificity of heme vibrational relaxation will require further experimental studies with individual side chain substitutions, the present experimental results are strongly supportive of the theoretical predictions made by Sagnella and Straub.²⁴

IV. Discussion

Hot Electronic Ground State Versus Multiple Electronic State Models. Ultrafast absorption spectroscopy has revealed complex wavelength-dependent optical transients in heme proteins.^{9,19,30} Two competing models have been proposed to interpret the observed spectral dynamics. One is based on the creation of a vibrationally “hot” electronic ground state of the photoproduct and its subsequent cooling,^{19,30,37,38} whereas the other model is based on the assumption of multiple electronically excited intermediate state species, having red-shifted absorption spectra, which decay to the final photoproduct ground state.^{9,29} In the work of Petrich et al.,⁹ the authors analyzed the optical transients at a few selected probe wavelengths and the variation

with probe wavelength was attributed to excited electronic intermediate states that absorb to the red (i.e., at 455 and 470 nm) of the Soret maximum. Within the context of this work, it is important to note that Petrich et al.,⁹ did acknowledge in the discussion of their data that the vibrationally hot ground electronic state model “cannot be unambiguously eliminated.”

The Soret and Q-band excited states of heme are known to be extremely short-lived, as is indicated by the broad absorption line shapes and extremely small fluorescence quantum yields.⁵¹ Various efforts have focused on clarifying why the nonradiative relaxation pathway is so efficient. In principle, femtosecond coherence spectroscopy (FCS) detects vibrational coherences associated with both the excited and ground electronic state species. However, such experiments yield a power spectrum that contains a strong Fe–His mode at 220 cm⁻¹, which is characteristic of the 5-coordinate electronic ground state.^{5,52} Moreover, in studies of MbNO, the prompt appearance of the 220 cm⁻¹ oscillation with essentially no phase delay⁵³ indicates that photolysis and evolution to the electronic ground state take place on a time scale that is significantly shorter than the 150 fs vibrational period of this mode. As a result of the absence of phase delay for the 220 cm⁻¹ mode, we have previously suggested⁵³ that ligand dissociation and creation of the 5-coordinate electronic ground state takes place within one-half of the Fe–NO vibrational period (<30 fs). It is also noteworthy that transient Raman experiments on MbCO find only ground-state normal modes of the unligated species within the system resolution of 2.3 ps.²⁵

It is significant that both the FCS experiments and the broadband continuum data presented here involve many different probe wavelengths. These measurements, especially those on the blue side of the Soret band, demonstrate that the multielectronic state model⁹ cannot account for the observed spectral relaxation without the fortuitous introduction of still more intermediate electronic states. For example, as can be seen in Figure 9 for MbNO, the optical transient recorded at 400 nm has a *rise* time of ~0.3 ps. This stands in marked contrast to what we would expect from the (multiple) excited electronic state model, which predicts that the signal observed at 400 nm should be similar in behavior to the signal measured at 420 nm (e.g. the initial nearly instantaneous rise of the transmission due to the bleach of MbNO followed by its decay to zero). The optical transient measured at 385 nm is also inconsistent with the multiple excited electronic state model, which predicts an antibleach as the ground electronic state of deoxyMb is created, having a *rise* time similar to the antibleach signal measured at 437 nm (see Figure 9). Experimental observation shows just the opposite, i.e., the signal measured at 385 nm is an antibleach with a *decay* time of about ~0.3 ps. On the other hand, these observations are consistent with the hypothesis of a “hot” (broadened and red-shifted) product absorption band superimposed on the reactant bleach background. Relaxation of a hot unphotodissociated 6-coordinate species¹⁹ is also consistent with the sign of the observed signal at 385 nm, so that the nearly instantaneous heating, and subsequent cooling, of both the 5- and 6-coordinate complexes must account for the observed relaxation at this wavelength. In contrast, the multielectronic state model would need to invoke still another excited intermediate state, absorbing in the blue, to be consistent with experimental the observations.

The two models also differ in their assumptions regarding quantum yield. The excited electronic state model assumes a unity quantum yield for each of the CO, O₂, and NO ligands and attributes the difference in the measurable dissociation yield

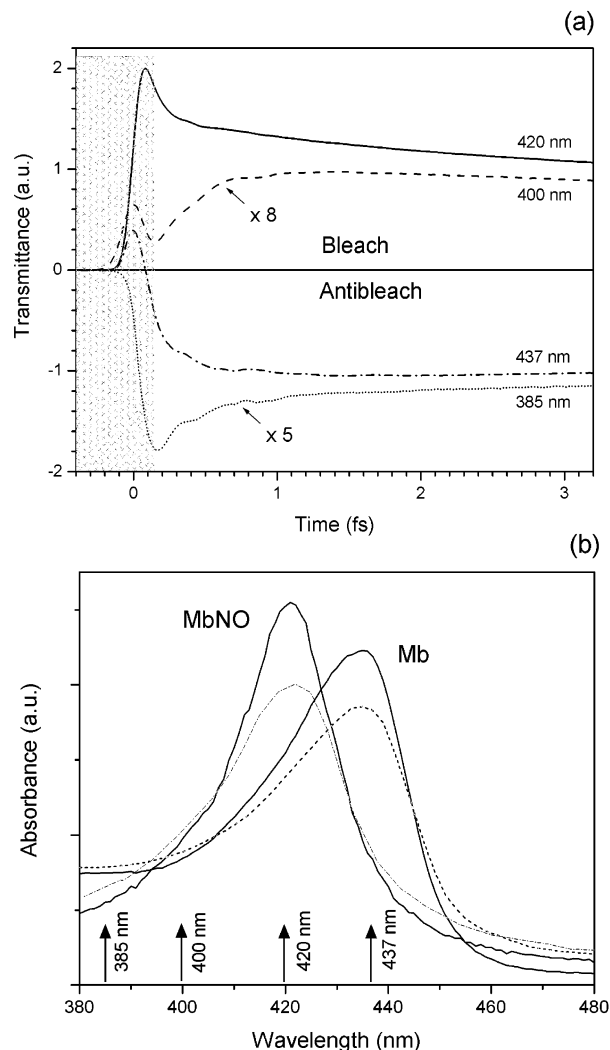


Figure 9. (Panel a) Selected optical transients of MbNO. The gray area on the left side shows the time region that covers the probe-before-pump signal and the coherence coupling response. This area is omitted from our analysis. (Panel b) A sketch of the photoproduct (Mb^* and MbNO^*) absorption spectra (dashed lines) as they evolve toward their respective equilibrium line shapes (solid lines) following photoexcitation of MbNO. The arrows denoted by 385, 400, 420, and 437 nm mark the excitation and detection wavelength of the optical transients presented in panel a.

to differences in the femtosecond geminate recombination of the ligands. On the other hand, we have recently demonstrated that the photodissociation quantum yield for MbNO and MbO_2 is not unity¹⁹ and the vibrational relaxation of the 6-coordinate photoproduct has been shown to contribute significantly to the spectral dynamics in the Soret region. In this previous work, we have suggested a relationship between the quantum yield, the ligand bending modes, and the equilibrium binding structure, which naturally accounts for the undissociated hot hexacoordinate photoproducts.¹⁹

Simulations. To demonstrate the applicability of the hot ground-state model to deoxyMb, we developed a simple model to simulate the observed transient spectra (Figure 10). The simulation is based on a homogeneous line shape convolved with an inhomogeneous non-Gaussian distribution⁵⁴ that yields an absorption band closely resembling the Soret absorption band of deoxy Mb. We utilize two adjustable parameters to control the overall spectrum of the photoexcited deoxyMb: the position of the absorption band and its width (i.e., the moments of the

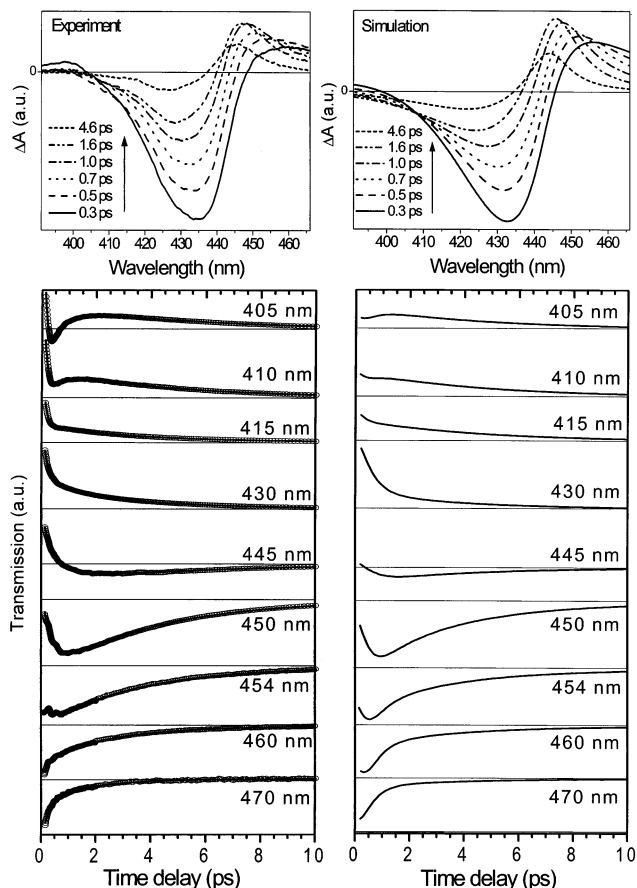


Figure 10. Transient spectra of deoxyMb measured with the 580-nm excitation (upper left) compared with the computer-simulated spectra (upper right) calculated using a red-shifted and broadened spectrum of the Mb photoproduct. In the calculations we use an exponential dependence of the photoproduct spectral shift from red to blue having a 4 ps time constant and an exponential spectral narrowing characterized by a 0.4 ps time constant. The lower left panels show the optical transients (from Figure 2) excited in the Soret band along with the simulated relaxations (lower right).

line shape). For simplicity, both of these parameters are modeled to change monoexponentially. When the calculated spectra are qualitatively compared with the experimental data, the best agreement is achieved if the change of the line shape position has a time constant of 4 ps and the width changes with a time constant of 400 fs. The overall shift of the spectrum is about 3–4 nm, whereas the full width at the shortest times is about 2.5 times broader than the equilibrium spectrum of Mb. The qualitative agreement between the simulations and the experimental data displayed in Figure 10 is striking and lends strong support to the vibrationally hot electronic ground state model. A more detailed demonstration of the hot dynamic line shape model is given by a comparison of calculated and experimentally measured single wavelength optical transients (lower part of Figure 10). One can see dramatic changes in the observed optical transient depending on the detection wavelength. It is important to note that, without the benefit of the broadband continuum spectra presented here, the single wavelength signals can easily be misinterpreted as arising from the population of multiple intermediate electronic states during the nonradiative decay that follows optical excitation.

Dynamic Line Shape Effects on Time-Resolved Resonance Raman Intensities. Another interesting and potentially important effect of the dynamic absorption line shape is its contribution to the time evolution of the resonance Raman scattering

intensities. Absorption spectra and Raman excitation profiles (REP, Raman scattering intensity as a function of excitation wavelength) are fundamentally linked through the imaginary and real parts of the polarizability tensor.^{55–57} For example, using the Kramers–Kronig transformation, the REP can be calculated directly from the measured absorption bands. In the case of a dynamic absorption line shape, the REP must also be dynamic. As the absorption spectrum characterizing a vibrationally hot species becomes broader, the Raman excitation photons probe an electronic resonance that is more “washed out”, leading to a relative diminution of the Raman scattering intensity at short times.

There are two basic factors that contribute to the temperature dependence of the resonance Raman scattering: the initial population of the vibrational mode being probed and the resonant absorption line shape of the molecule. For harmonic systems, these two factors can be explicitly decoupled:

$$I_i^\pm \propto \left(\bar{n}_i + \frac{1}{2} \pm \frac{1}{2} \right) |S_i| |\phi_T(\tilde{\nu}) - \phi_T(\tilde{\nu} \mp \tilde{\nu}_i)|^2 \quad (3)$$

where \bar{n}_i is the thermally averaged vibrational population, or Bose–Einstein factor,

$$\bar{n}_i = (e^{\tilde{\nu}_i/kT} - 1)^{-1} \quad (4)$$

and $\phi_T(\tilde{\nu})$ is the complex (and temperature dependent) line shape function (the + and – superscripts denote Stokes and anti-Stokes scattering, respectively). The quantity $\phi_T(\tilde{\nu})$ can be found from a Kramers–Kronig transform using the imaginary part, which is given by the temperature-dependent absorption line shape, $\sigma_A(\tilde{\nu}, T)$:

$$\phi_T(\tilde{\nu}) = \frac{1}{\pi} P \int_{-\infty}^{\infty} d\tilde{\nu}' \frac{\sigma_A(\tilde{\nu}', T)}{\tilde{\nu}'(\tilde{\nu}' - \tilde{\nu})} + i \frac{\sigma_A(\tilde{\nu}, T)}{\tilde{\nu}} \quad (5)$$

It is important not to neglect the dynamics of the complex line shape function when attempting to determine transient vibrational temperatures using the Stokes and anti-Stokes resonance Raman intensities. The Bose–Einstein factor obviously plays an important role, but the dynamics of the complex resonance line shape function also leads to important time dependent changes in the Raman intensities.

For example, time-resolved resonance Raman spectroscopy has been used to monitor the vibrational relaxation of the heme upon photodissociation of the CO ligand.^{25,26} In these studies, the anti-Stokes ν_4 mode intensity was found to relax with a time constant of 1.9 ps, which was interpreted as a direct measure of vibrational population decay [i.e., $I_4^-(t)$ was implicitly assumed to be proportional to $\bar{n}_i(t)$ in eq 3]. In these studies,^{25–27} the time-independent equilibrium line shape function was used and the effect of dynamics in the complex line shape, $\phi_T(\tilde{\nu}, t)$, was neglected. To demonstrate the importance of such effects, we use the dynamic absorption spectra presented here and apply Kramers–Kronig transform theory to calculate its effect on the dynamics of the REP.

For the purpose of demonstration, we implicitly assume Boltzmann statistics, even though this is probably unjustified at the earliest times. Nevertheless, the present calculations can potentially serve as a guide for a more precise extraction of vibrational temperatures using resonance Raman scattering intensities. In Figure 11, we have taken the fit of Mizutani and Kitagawa²⁵ for the anti-Stokes ν_4 intensity (open circles) and used it to determine $\bar{n}_4(t)$ by explicitly taking into account the dynamics of the complex line shape function, $\phi_T(\tilde{\nu}, t)$, as

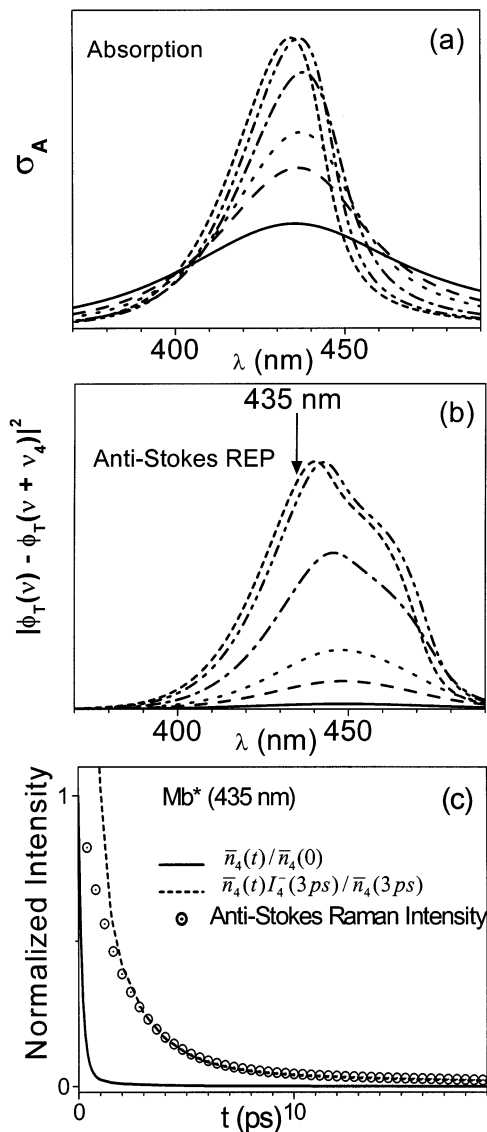


Figure 11. (Panel a) Simulated dynamic absorption spectra of the vibrationally excited myoglobin with time delays of 0, 0.3, 0.5, 1, 3, and 10 ps. (Panel b) The corresponding anti-Stokes resonance Raman excitation line shapes for the ν_4 mode. For these calculations, the inhomogeneity in the absorption spectrum is first deconvolved prior to performing the Kramers–Kronig transform.⁵⁷ Raman excitation line shapes are calculated using eqs 3–5 and then reconvolved with the inhomogeneous distribution. (Panel c) The experimentally measured²⁵ anti-Stokes relaxation of the ν_4 mode Raman intensity, $I_4^-(t)$, which is used to find $\bar{n}_4(t)$ using the dynamic line shape function (and eq 3). The quantities $\bar{n}_4(t)/\bar{n}_4(0)$ and $\bar{n}_4(t)I_4^-(3 \text{ ps})/\bar{n}_4(3 \text{ ps})$ are plotted in the figure to normalize the plots at $t = 0$ and 3 ps.

calculated from eq 5 at discrete time points. The result is shown as a solid line in Figure 11. In addition to the time dependent Raman intensity and Bose–Einstein factor, Figure 11 also contains the simulated time dependent absorption and REP line shapes that were used in the calculations. The difference between the time dependent decay of the anti-Stokes Raman intensity (open circles, $I_4^-(t)$) and the actual vibrational population ($\bar{n}_4(t)$, given by solid line) is most significant at the earliest times. To show how the signal scales at the longer times we have also renormalized the calculated values for $\bar{n}_4(t)$ to the data at 3ps (shown as a dashed line). The time constant for the decay of $I_4^-(t)$ is ~ 2 ps, while that for $\bar{n}_4(t)$ is ~ 300 fs. This example shows how the simple use of $I_4^-(t)$ to measure $\bar{n}_4(t)$ may significantly overestimate the true value of the thermal decay

time when the laser excitation wavelength is resonant with a thermally broadened dynamic lineshape. On the other hand, it is difficult to obtain Raman data on time scales shorter than ~ 1 ps, so that the very rapid components of the cooling signal may be difficult to detect. This difficulty, along with the potentially non-Boltzmann nature of the process, leads to additional ambiguity in extracting the correct timescales for cooling. Finally, it is worth remembering that the time dependent decay of $\bar{n}_i(t)$ scales exponentially with the inverse of vibrational temperature (e.g., see eq 4) so that fits to $\bar{n}_i(t)$ do not directly give time constants for the decay of the Boltzmann temperature. Most importantly, the results shown in Figure 11 clearly demonstrate the need for properly considering the time dependence of the resonant line shape function when attempting to extract $\bar{n}_i(t)$ from time-resolved Raman data.

V. Summary

The present work investigates the flow of photoexcitation energy in biomolecules. The transient absorption spectra of various oxidation and ligation states of myoglobin all display an initially broad and red-shifted photoproduct absorption spectrum. The results show this to be a signature of the relaxation of vibrationally hot species. The broadband continuum data support the vibrational relaxation model, which in conjunction with femtosecond coherence studies^{5,28} indicates an almost instantaneous (< 30 fs) decay to the electronic ground state of the photoproduct. The results are not consistent with the assignment of the relaxation to a multiple electronic state pathway⁹ unless additional electronic states, absorbing to the blue as well as to the red of the Soret band, are postulated. The photoexcitation energy appears to be initially deposited locally on the heme group. By using samples with modified local heme environments (e.g., the H93G mutant and the iron-porphine reconstituted myoglobin), we find that a vibrational relaxation path through the van der Waals contacts at the heme periphery is more important than through the single Fe-His covalent bond between the heme and the protein matrix. Finally, we demonstrate that a dynamically evolving absorption band leads directly to a time dependent complex line shape function and REP, which must be considered along with the Bose-Einstein factor when attempting to extract a time dependent vibrational temperature from picosecond resonance Raman data.

Acknowledgment. We dedicate this paper to the memory of Prof. A. C. Albrecht and thank him for his many contributions to our understanding of resonance Raman scattering. This work was supported by grants from NIH (DK35090) and NSF (MCB9904516).

References and Notes

- (1) Antonini, E.; Brunori, M. *Hemoglobin and myoglobin in their reactions with ligands*; North-Holland Publishing Co.: Amsterdam-London, 1971.
- (2) Brunori, M. *Trends Biochem. Sci.* **2001**, *26*, 209–210.
- (3) Eich, R. F.; Li, T. S.; Lemon, D. D.; Doherty, D. H.; Curry, S. R.; Aitken, J. F.; Mathews, A. J.; Johnson, K. A.; Smith, R. D.; Phillips, G. N.; Olson, J. S. *Biochemistry* **1996**, *35*, 6976–6983.
- (4) Frauenfelder, H.; McMahon, B. H.; Austin, R. H.; Chu, K.; Groves, J. T. *Proc. Natl. Acad. Sci. U.S.A.* **2001**, *98*, 2370–2374.
- (5) Zhu, L. Y.; Sage, J. T.; Champion, P. M. *Science* **1994**, *266*, 629–632.
- (6) Zhu, L.; Zhong, G.; Champion, P. M. *Femtochemistry: Ultrafast Chemical and Physical Processes in Molecular Systems*; World Scientific: Singapore, 1996; pp 387–393.
- (7) Franzen, S.; Bohn, B.; Poyart, C.; Martin, J. L. *Biochemistry* **1995**, *34*, 1224–1237.
- (8) Anfinrud, P. A.; Han, C.; Hochstrasser, R. M. *Proc. Natl. Acad. Sci. U.S.A.* **1989**, *86*, 8387–8391.
- (9) Petrich, J. W.; Poyart, C.; Martin, J. L. *Biochemistry* **1988**, *27*, 4049–4060.
- (10) Ansari, A.; DiIorio, E. E.; Dlott, D. D.; Frauenfelder, H.; Iben, I. E. T.; Langer, P.; Roder, H.; Sauke, T. B.; Shyamsunder, E. *Biochemistry* **1986**, *25*, 3139–3146.
- (11) Ogilvie, J. P.; Plazenet, M.; Dadusc, G.; Miller, R. J. D. *J. Phys. Chem. B* **2002**, *106*, 10460–10467.
- (12) Cornelius, P. A.; Hochstrasser, R. M.; Steele, A. W. *J. Mol. Biol.* **1983**, *163*, 119–128.
- (13) Austin, R. H.; Beeson, K.; Eisenstein, L.; Frauenfelder, H.; Gunsalus, I. C. *Biochemistry* **1975**, *14*, 5355–5373.
- (14) Henry, E. R.; Sommer, J. H.; Hofrichter, J.; Eaton, W. A. *J. Mol. Biol.* **1983**, *166*, 443–451.
- (15) Walda, K. N.; Liu, X. Y.; Sharma, V. S.; Magde, D. *Biochemistry* **1994**, *33*, 2198–2209.
- (16) Tian, W. D.; Sage, J. T.; Srajer, V.; Champion, P. M. *Phys. Rev. Lett.* **1992**, *68*, 408–411.
- (17) Champion, P. M. *J. Raman Spectrosc.* **1992**, *23*, 557–567.
- (18) Jongeward, K. A.; Magde, D.; Taube, D. J.; Marsters, J. C.; Traylor, T. G.; Sharma, V. S. *J. Am. Chem. Soc.* **1988**, *110*, 380–387.
- (19) Ye, X.; Demidov, A. A.; Champion, P. M. *J. Am. Chem. Soc.* **2002**, *124*, 5914–5924.
- (20) Miller, R. J. D. *Annu. Rev. Phys. Chem.* **1991**, *42*, 581–614.
- (21) Li, P.; Champion, P. M. *Biophys. J.* **1994**, *66*, 430–436.
- (22) Li, P.; Sage, J. T.; Champion, P. M. *J. Chem. Phys.* **1992**, *97*, 3214–3227.
- (23) Simpson, M. C.; Peterson, E. S.; Shannon, C. F.; Eads, D. D.; Friedman, J. M.; Cheatum, C. M.; Ondrias, M. R. *J. Am. Chem. Soc.* **1997**, *119*, 5110–5117.
- (24) Sagnella, D. E.; Straub, J. E. *J. Phys. Chem. B* **2001**, *105*, 7057–7063.
- (25) Mizutani, Y.; Kitagawa, T. *Science* **1997**, *278*, 443–446.
- (26) Mizutani, Y.; Kitagawa, T. *Chem. Rec.* **2001**, *1*, 258–275.
- (27) Lingle, R.; Xu, X. B.; Zhu, H. P.; Yu, S. C.; Hopkins, J. B. *J. Phys. Chem.* **1991**, *95*, 9320–9331.
- (28) Rosca, F.; Kumar, A. T. N.; Ye, X.; Sjodin, T.; Demidov, A. A.; Champion, P. M. *J. Phys. Chem.* **2000**, *104*, 4280–4290.
- (29) Franzen, S.; Kiger, L.; Poyart, C.; Martin, J. L. *Biophys. J.* **2001**, *80*, 2372–2385.
- (30) Kholodenko, Y.; Volk, M.; Gooding, E.; Hochstrasser, R. A. *Chem. Phys.* **2000**, *259*, 71–87.
- (31) Lim, M. H.; Jackson, T. A.; Anfinrud, P. A. *J. Phys. Chem.* **1996**, *100*, 12043–12051.
- (32) Shreve, A. P.; Franzen, S.; Simpson, M. C.; Dyer, R. B. *J. Phys. Chem. B* **1999**, *37*, 7969–7975.
- (33) Kovalenko, S. A.; Schanz, R.; Farztdinov, V. M.; Hennig, H.; Ernsting, N. P. *Chem. Phys. Lett.* **2000**, *323*, 312–322.
- (34) Elsaesser, T.; Kaiser, W. *Annu. Rev. Phys. Chem.* **1991**, *42*, 83–107.
- (35) Rodriguez, J.; Kirmaier, C.; Holten, D. *J. Chem. Phys.* **1991**, *94*, 6020–6029.
- (36) Rodriguez, J.; Holten, D. *J. Chem. Phys.* **1990**, *92*, 5944–5950.
- (37) Rodriguez, J.; Holten, D. *J. Chem. Phys.* **1989**, *91*, 3525–3531.
- (38) Rodriguez, J.; Westerfield, W.; Whiteley, B.; Kirmaier, C.; Holten, D. *J. Lumin.* **1994**, *60–1*, 507–510.
- (39) Barrick, D. *Biochemistry* **1994**, *33*, 6546–6554.
- (40) DePillis, G. D.; Decatur, S. M.; Barrick, D.; Boxer, S. G. *J. Am. Chem. Soc.* **1994**, *116*, 6981–6982.
- (41) Neya, S.; Funasaki, N.; Sato, T.; Igarashi, N.; Tanaka, N. *J. Biol. Chem.* **1993**, *268*, 8935–8942.
- (42) Wang, W.; Ye, X.; Demidov, A. A.; Rosca, F.; Sjodin, T.; Cao, W.; Sheeran, M.; Champion, P. M. *J. Phys. Chem. B* **2000**, *104*, 10789–10801.
- (43) Skilling, J.; Bryan, R. K. *Mon. Not. R. Astron. Soc.* **1984**, *211*, 111–124.
- (44) Stephenson, D. S. *Prog. NMR Spectrosc.* **1988**, *20*, 515–626.
- (45) Press, W. H.; Teukolsky, S. A.; Vetterling, W. T.; Flannery, B. P. *Numerical Recipes in C*, 2nd ed.; Cambridge University Press: Cambridge, 1992.
- (46) Kumar, A. T. N.; Zhu, L.; Christian, J. F.; Demidov, A. A.; Champion, P. M. *J. Phys. Chem. B* **2001**, 7847–7856.
- (47) Cao, W.; Christian, J. F.; Champion, P. M.; Rosca, F.; Sage, J. T. *Biochemistry* **2001**, *40*, 5728–5737.
- (48) Henry, E. R.; Eaton, W. A.; Hochstrasser, R. M. *Proc. Natl. Acad. Sci. U.S.A.* **1986**, *83*, 8982–8986.
- (49) Bucher, T.; Kaspers, J. *Biochim. Biophys. Acta* **1947**, *1*, 21–34.
- (50) Rosca, F.; Kumar, A. T. N.; Ionascu, D.; Ye, X.; Demidov, A. A.; Sjodin, T.; Wharton, D.; Barrick, D.; Sligar, S. G.; Yonetani, T.; Champion, P. M. *J. Phys. Chem. A* **2002**, *106*, 3540–3552.

- (51) Champion, P. M.; Lange, R. *J. Chem. Phys.* **1980**, *73*, 5947–5957.
- (52) Champion, P. M.; Rosca, F.; Wang, W.; Kumar, A. T. N.; Christian, J.; Demidov, A. *Proc. SPIE in "Laser Techniques for Condensed-Phase and Biological Systems"* **1998**, *3273*, 80–89.
- (53) Rosca, F.; Kumar, A. T. N.; Ionascu, D.; Sjodin, T.; Demidov, A. A.; Champion, P. M. *J. Chem. Phys.* **2001**, *114*, 10884–10898.
- (54) Srajer, V.; Schomacker, K. T.; Champion, P. M. *Phys. Rev. Lett.* **1986**, *57*, 1267–1270.
- (55) Champion, P. M.; Albrecht, A. C. *Annu. Rev. Phys. Chem.* **1982**, *33*, 353–376.
- (56) Champion, P. M.; Albrecht, A. C. *J. Chem. Phys.* **1980**, *72*, 6498.
- (57) Stallard, B. R.; Champion, P. M.; Callis, P. R.; Albrecht, A. C. *J. Chem. Phys.* **1983**, *78*, 712–722.